

ROBUST MULTIGRID FOR HIGH-ORDER DISCONTINUOUS GALERKIN METHODS: A FAST POISSON SOLVER SUITABLE FOR HIGH-ASPECT RATIO CARTESIAN GRIDS

JÖRG STILLER

Technische Universität Dresden, Institute of Fluid Mechanics and Center for Advancing Electronics Dresden, 01062 Dresden, Germany

ABSTRACT. We present a polynomial multigrid method for nodal interior penalty and local discontinuous Galerkin formulations of the Poisson equation on Cartesian grids. For smoothing we propose two classes of overlapping Schwarz methods. The first class comprises element-centered and the second face-centered methods. Within both classes we identify methods that achieve superior convergence rates, prove robust with respect to the mesh spacing and the polynomial order, at least up to $P = 32$. Consequent structure exploitation yields a computational complexity of $O(PN)$, where N is the number of unknowns. Further we demonstrate the suitability of the face-centered method for element aspect ratios up to 32.

1. INTRODUCTION

High-order discretization methods are exciting because of their promise to deliver higher accuracy at lower cost than first and second order methods. Much confidence has been put in the discontinuous Galerkin (DG) method because it combines multiple desirable properties of finite element and finite volume methods, including geometric flexibility, variable approximation order, straightforward adaptivity and suitability for conservation laws [6, 19]. Traditionally, DG methods have been used in the numerical solution of hyperbolic and convection-dominated problems. Nevertheless, the need for implicit diffusion schemes and application to other problem classes, such as incompressible flow and elasticity, led to a growing interest in DG methods and related solution techniques for elliptic equations [2, 30].

The most efficient elliptic solvers are based on multigrid (MG) techniques and can be classified into polynomial or p -MG [11, 17, 18], geometric or h -MG [10, 15, 22, 23, 25, 31] or, combining both concepts, hp -MG [1, 35], and algebraic MG [3, 28, 29, 32]. Apart from their different coarsening strategy, polynomial and geometric multigrid are closely related to each other and can be applied with the same smoothing methods. Early work on p -MG goes back to Helenbrook and coworkers [17, 18] who explored various smoothers

E-mail address: joerg.stiller@tu-dresden.de.

Key words and phrases. Discontinuous Galerkin, elliptic problems, multigrid method, Schwarz method, Krylov acceleration, Cartesian grids.

for DG formulations of the Poisson equation. For isotropic grids they identified block Gauss-Seidel as the best choice, whereas more expensive line smoothing proved necessary on high-aspect-ratio grids. At about the same time, Gopalakrishnan and Kanschat [15] developed h -MG preconditioners for Poisson and convection-diffusion problems, which also use element-based block-Gauss-Seidel methods for smoothing. Kanschat [22, 23] extended this approach to locally refined Cartesian grids in two and three space dimensions. In both cases, polynomial and geometric multigrid, block-Gauss-Seidel smoothing yields acceptable convergence rates for low to moderate polynomial degrees, e.g. $\rho \approx 0.5$ with one pre-smoothing for $P = 4$. However, the convergence degrades with increasing P , which renders the approach unfeasible for higher polynomial degrees.

Several researchers proposed algebraic multigrid methods for various DG formulations of elliptic equations. Olson and Schroder [28] presented a preconditioned conjugate gradient (PCG) method based on smoothed aggregation. Using block relaxation combined with energy-minimizing prolongation it attains mesh independent convergence rates corresponding to residual reductions of about 0.3 per smoothing step for $P \leq 6$, but degrades with increasing approximation order. Bastian et al. [3] proposed a non-smoothed aggregation approach. For smoothing they use block relaxations which operate on extended aggregates and, hence, can be regarded as overlapping Schwarz methods. This approach yields by far the most efficient DG-MG method reported until now. The method proved robust with respect to the polynomial order, up to at least $P = 6$, though the iteration count exhibits a logarithmic dependence on the mesh spacing. For the DG method of Oden, Babuška and Baumann it achieved convergence rates of $\rho \approx 0.002$ with one pre- and post-smoothing, which corresponds to a residual reduction of approximately 0.05 in one step. The approach was also shown to work with symmetric and non-symmetric interior penalty methods, although it required nearly twice as many iterations in the latter case. A possible drawback is the rise of cost with increasing polynomial order. The authors did not specify the complexity of their algorithm, however the solver runtimes indicate that the cost per unknown grows as P^3 in 2D and P^5 in 3D.

To the best of our knowledge, none of the proposed MG methods is robust with respect to both, the polynomial order and the mesh spacing. Computational complexity and robustness against high aspect ratios are further issues that need to be considered to strengthen the competitiveness of DG methods for elliptic equations. As a step into that direction we present a new p -multigrid method for interior penalty and local discontinuous Galerkin discretizations of the Poisson equation on Cartesian grids. Our approach is motivated and strongly influenced by previous work dedicated to the continuous spectral element method [16, 20, 26, 33]. We propose two classes of multiplicative and weighted additive Schwarz methods, which use an adjustable overlap depending on the polynomial level. The first class comprises element-centered and the second face-centered methods. Within both classes we identify methods that achieve superior convergence rates, prove robust with respect to the mesh spacing and the polynomial order and reach a computational complexity of $O(PN)$, where N is the number of unknowns. Further we demonstrate the suitability of the face-centered method for high element aspect ratios.

The remainder of the paper is organized as follows: In the next section we derive a unified nodal DG formulation of the Poisson problem comprising the symmetric interior penalty method and the local discontinuous Galerkin method. Then we describe the solution methods, i.e. Schwarz, multigrid und inexact PCG, in Section 3. Section 4 presents the numerical experiments and Section 5 concludes the paper.

2. DISCONTINUOUS GALERKIN METHOD

2.1. Problem definition. As a model problem we consider the Poisson equation

$$-\nabla^2 u = f \quad (1)$$

in the rectangular periodic domain $\Omega = [0, l_1] \times [0, l_2]$. By introducing the flux vector $\boldsymbol{\sigma} = \nabla u$, the problem can be rewritten into the first-order system

$$\boldsymbol{\sigma} = \nabla u, \quad (2a)$$

$$-\nabla \cdot \boldsymbol{\sigma} = f. \quad (2b)$$

This form serves as the starting point for the discontinuous Galerkin method.

2.2. Spatial discretization. The domain Ω is decomposed into $N_E = N_{E,1} \times N_{E,2}$ rectangular elements

$$\Omega^{m_1, m_2} = (x_1^{m_1-1/2}, x_1^{m_1+1/2}) \times (x_2^{m_2-1/2}, x_2^{m_2+1/2})$$

with dimensions $\Delta x_d^{m_d} = x_d^{m_d+1/2} - x_d^{m_d-1/2}$ for $d = 1, 2$. Each element is mapped to the standard region $(-1, 1)^2$ by

$$\xi_d^{m_d}(x) = \frac{2}{\Delta x_d^{m_d}}(x_d - x_d^{m_d-1/2}) - 1.$$

For simplicity we use the array notations $\mathbf{m} = (m_1, m_2)$, $\mathbf{x} = (x_1, x_2)$ and $\boldsymbol{\xi} = (\xi_1, \xi_2)$ where possible.

Let $\{\varphi_i(\xi)\}_{i=0}^P$ be a polynomial basis of degree P in the interval $[-1, 1]$. Using a tensor-product ansatz the solution to (2) can be approximated in $\Omega^{\mathbf{m}}$ as

$$u_h(\mathbf{x})|_{\Omega^{\mathbf{m}}} = u^{\mathbf{m}}(\boldsymbol{\xi}^{\mathbf{m}}(\mathbf{x})) = \sum_{i,j=0}^P u_{ij}^{\mathbf{m}} \varphi_i(\xi_1) \varphi_j(\xi_2) \quad (3)$$

and

$$\boldsymbol{\sigma}_h(\mathbf{x})|_{\Omega^{\mathbf{m}}} = \boldsymbol{\sigma}^{\mathbf{m}}(\boldsymbol{\xi}^{\mathbf{m}}(\mathbf{x})) = \sum_{i,j=0}^P \boldsymbol{\sigma}_{ij}^{\mathbf{m}} \varphi_i(\xi_1) \varphi_j(\xi_2). \quad (4)$$

The global solution u_h and the fluxes $\boldsymbol{\sigma}_h$ belong to the function spaces

$$V_h = \left\{ v \in L^2(\Omega) : v|_{\Omega^{\mathbf{m}}} \in Q_p(\Omega^{\mathbf{m}}) \quad \forall \Omega^{\mathbf{m}} \subset \Omega \right\} \quad \text{and} \\ \boldsymbol{\Sigma}_h = \left\{ \boldsymbol{\tau} \in [L^2(\Omega)]^2 : \boldsymbol{\tau}|_{\Omega^{\mathbf{m}}} \in [Q_p(\Omega^{\mathbf{m}})]^2 \quad \forall \Omega^{\mathbf{m}} \subset \Omega \right\},$$

respectively, where $Q_p(\Omega^{\mathbf{m}})$ is the space spanned by the tensor product polynomials $x_1^k y_2^l$ with $0 \leq k, l \leq P$ in $\Omega^{\mathbf{m}}$.

2.3. Elemental DG formulation. Following Cockburn and Shu [5] we consider discontinuous Galerkin formulations of the form: Find $u_h \in V_h$ and $\boldsymbol{\sigma}_h \in \boldsymbol{\Sigma}_h$ such that for all $\Omega^m \subset \Omega$

$$\int_{\Omega^m} \boldsymbol{\tau} \cdot \boldsymbol{\sigma}_h \, d\Omega = - \int_{\Omega^m} (\nabla \cdot \boldsymbol{\tau}) u_h \, d\Omega + \int_{\partial\Omega^m} \boldsymbol{\tau} \cdot \hat{\mathbf{n}} \, d\Gamma \quad \forall \boldsymbol{\tau} \in [Q_p(\Omega^m)]^2, \quad (5a)$$

$$\int_{\Omega^m} \nabla v \cdot \boldsymbol{\sigma}_h \, d\Omega = \int_{\Omega^m} v f \, d\Omega + \int_{\partial\Omega^m} v \hat{\boldsymbol{\sigma}} \cdot \mathbf{n} \, d\Gamma \quad \forall v \in Q_p(\Omega^m), \quad (5b)$$

where the numerical fluxes \hat{u} and $\hat{\boldsymbol{\sigma}}$ are approximations to u and to $\boldsymbol{\sigma} = \nabla u$, respectively, on the element boundary $\partial\Omega^m$. To concretize the numerical fluxes we need some additional notation. For given functions $v \in V_h$, $\boldsymbol{\tau} \in \boldsymbol{\Sigma}_h$ let v^- , $\boldsymbol{\tau}^-$ and v^+ , $\boldsymbol{\tau}^+$ denote the interior and exterior traces on $\partial\Omega^m$, respectively. Now we define the average and jump operators by

$$\{v\} = \frac{1}{2} (v^- + v^+), \quad \{\boldsymbol{\tau}\} = \frac{1}{2} (\boldsymbol{\tau}^- + \boldsymbol{\tau}^+), \quad (6a)$$

$$[[v]] = (v^- - v^+) \mathbf{n}, \quad [[\boldsymbol{\tau}]] = (\boldsymbol{\tau}^- - \boldsymbol{\tau}^+) \cdot \mathbf{n}. \quad (6b)$$

We remark that, despite element oriented notation, these definitions are in fact element independent and equivalent to those given in [2].

For constructing the numerical fluxes we consider the interior penalty method (IP) and the local discontinuous Galerkin method (LDG). We closely follow the notation used in [2]. With IP the numerical fluxes take the form

$$\hat{u} = \{u\}, \quad (7a)$$

$$\hat{\boldsymbol{\sigma}} = \{\nabla u_h\} - \mu_{\text{IP}} [[u_h]] \quad (7b)$$

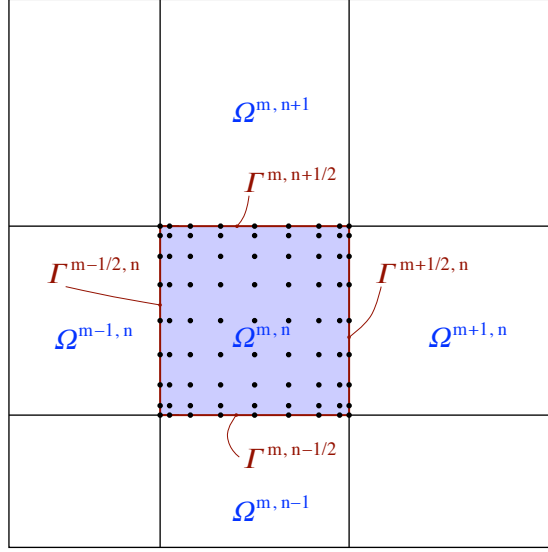
and with LDG

$$\hat{u} = \{u_h\} - \boldsymbol{\beta} \cdot [[u_h]], \quad (8a)$$

$$\hat{\boldsymbol{\sigma}} = \{\boldsymbol{\sigma}_h\} + \boldsymbol{\beta} [[\boldsymbol{\sigma}_h]] - \mu_{\text{LDG}} [[u_h]]. \quad (8b)$$

Here μ_{IP} and μ_{LDG} are positive penalty functions that are defined on the edges and typically piecewise constant. According to [2], $\mu_{\text{LDG}} > 0$ is sufficient for stability with LDG, whereas no general stability threshold is known for IP. The auxiliary parameter $\boldsymbol{\beta}$ can be used to improve the sparsity of the stiffness matrix [5]. Moreover, Cockburn et al. [7] devised a special form of $\boldsymbol{\beta}$ which yields superconvergence in the L^2 norm when used with Cartesian grids. This form includes constant vectors with components satisfying $|\beta_d| = 1/2$. As a possible drawback, however, any non-trivial choice of $\boldsymbol{\beta}$ also implies a directional bias and thus breaks the symmetry of diffusive transport.

2.4. Discrete equations. In the following we constrain ourselves to nodal bases formed by the Lagrange polynomials to the Gauss-Lobatto-Legendre (GLL) quadrature points $\{\eta_i\}$ in the standard interval $[-1, 1]$, see e.g. [9, 19, 24]. The GLL quadrature is used for evaluating integrals over element domains, which yields a diagonal mass matrix without degrading the overall accuracy of the method.

FIGURE 1. Element domain with collocation points of order $P = 8$.

First we derive explicit expressions for the discrete fluxes. Application of the divergence theorem to (5a) yields the equivalent form

$$\int_{\Omega^m} \boldsymbol{\tau} \cdot \boldsymbol{\sigma}_h \, d\Omega = \int_{\Omega^m} \boldsymbol{\tau} \cdot \nabla u_h \, d\Omega + \int_{\partial\Omega^m} \boldsymbol{\tau} \cdot (\hat{u} - u^-) \mathbf{n} \, d\Gamma.$$

Substituting the numerical flux (7a) or (8a) for \hat{u} , respectively, we obtain

$$\int_{\Omega^m} \boldsymbol{\tau} \cdot \boldsymbol{\sigma}_h \, d\Omega = \int_{\Omega^m} \boldsymbol{\tau} \cdot \nabla u_h \, d\Omega - \int_{\partial\Omega^m} \left(\frac{1}{2} + \boldsymbol{\beta} \cdot \mathbf{n} \right) \boldsymbol{\tau} \cdot \llbracket u \rrbracket \, d\Gamma,$$

where $\boldsymbol{\beta}$ vanishes for IP and is constant for LDG. Choosing $\boldsymbol{\tau}|_{\Omega^m} = \varphi_i(\xi_1)\varphi_j(\xi_2)\mathbf{e}_d$, substituting the approximate solution (3, 4) and evaluating the integrals by means of GLL quadrature leads to

$$\mathbf{M}^m \boldsymbol{\sigma}^m = \mathbf{M}^m \nabla \mathbf{u}^m + \sum_{\gamma=1}^4 \left(\frac{1}{2} + \boldsymbol{\beta} \cdot \mathbf{n}_\gamma \right) \mathbf{M}_\gamma (\mathbf{u}_\gamma^+ - \mathbf{u}_\gamma^-) \mathbf{n}_\gamma, \quad (9)$$

where

$$M_{ij,kl}^m = \frac{\Delta x_1^{m_1} \Delta x_2^{m_2}}{4} \rho_i \rho_j \delta_{ik} \delta_{jl}$$

is the element mass matrix,

$$(\nabla u)_{ij}^m = \left[\begin{array}{c} \frac{2}{\Delta x_1^{m_1}} \sum_{p=0}^P D_{ip} u_{pj}^m \\ \frac{2}{\Delta x_2^{m_2}} \sum_{q=0}^P D_{jq} u_{iq}^m \end{array} \right], \quad (10)$$

the solution gradient at the GLL points, ρ_i the quadrature weights, and $D_{ik} = \varphi'_k(\eta_i)$ the standard differentiation matrix [9, 24]. Note that the latter and the weights apply to both coordinate directions. The last term in (9) comprises the contributions of the boundary edges (see Fig. 1). Table 1 summarizes the corresponding operators and variables.

TABLE 1. Element boundary operators and variables.

γ	edge	\mathbf{n}_γ	\mathbf{M}_γ	\mathbf{u}_γ^-	\mathbf{u}_γ^+
1	$\Gamma^{m_1-1/2, m_2}$	$-\mathbf{e}_1$	$\frac{1}{2}\Delta x_2^{m_2}\rho_j\delta_{i0}\delta_{jq}$	$u_{0q}^{\mathbf{m}}$	$u_{Pq}^{m_1-1, m_2}$
2	$\Gamma^{m_1, m_2-1/2}$	$-\mathbf{e}_2$	$\frac{1}{2}\Delta x_1^{m_1}\rho_i\delta_{ip}\delta_{j0}$	$u_{p0}^{\mathbf{m}}$	$u_{pP}^{m_1, m_2-1}$
3	$\Gamma^{m_1+1/2, m_2}$	\mathbf{e}_1	$\frac{1}{2}\Delta x_2^{m_2}\rho_j\delta_{iP}\delta_{jq}$	$u_{Pq}^{\mathbf{m}}$	$u_{0q}^{m_1+1, m_2}$
4	$\Gamma^{m_1, m_2+1/2}$	\mathbf{e}_2	$\frac{1}{2}\Delta x_1^{m_1}\rho_i\delta_{ip}\delta_{jP}$	$u_{pP}^{\mathbf{m}}$	$u_{0p}^{m_1, m_2+1}$

Substituting these in (9) and multiplying the inverse mass matrix yields the flux vector coefficients

$$\begin{aligned} \boldsymbol{\sigma}_{ij}^{\mathbf{m}} &= (\nabla u)_{ij}^{\mathbf{m}} \\ &+ \left[\frac{1-2\beta_1}{\Delta x_1^{m_1}\rho_0}\delta_{i0}\left(u_{0j}^{m_1, m_2} - u_{Pj}^{m_1-1, m_2}\right) + \frac{1+2\beta_1}{\Delta x_1^{m_1}\rho_P}\delta_{iP}\left(u_{0j}^{m_1+1, m_2} - u_{Pj}^{m_1, m_2}\right) \right. \\ &\quad \left. + \frac{1-2\beta_2}{\Delta x_2^{m_2}\rho_0}\delta_{j0}\left(u_{i0}^{m_1, m_2} - u_{iP}^{m_1, m_2-1}\right) + \frac{1+2\beta_2}{\Delta x_2^{m_2}\rho_P}\delta_{jP}\left(u_{i0}^{m_1, m_2+1} - u_{iP}^{m_1, m_2}\right) \right]. \end{aligned} \quad (11)$$

Equations (10, 11) immediately lead to explicit expressions for the numerical fluxes $\hat{\boldsymbol{\sigma}}$ defined by (7b) and (8b), respectively. As the discrete equations require only the flux normal to the boundary, it is sufficient to consider the x_1 -component at edge $\Gamma^{m_1+1/2, m_2}$ and, correspondingly, the x_2 -component at $\Gamma^{m_1, m_2+1/2}$. For IP it follows

$$\begin{aligned} \hat{\sigma}_{1,j}^{m_1+1/2, m_2} &= \frac{1}{\Delta x_1^{m_1}} \sum_{k=0}^P D_{Pk} u_{kj}^{m_1, m_2} + \frac{1}{\Delta x_1^{m_1+1}} \sum_{l=0}^P D_{0l} u_{lj}^{m_1+1, m_2} \\ &\quad + \mu_{\text{IP}}^{m_1+1/2, m_2} \left(u_{0j}^{m_1+1, m_2} - u_{Pj}^{m_1, m_2} \right), \end{aligned} \quad (12a)$$

$$\begin{aligned} \hat{\sigma}_{2,i}^{m_1, m_2+1/2} &= \frac{1}{\Delta x_2^{m_2}} \sum_{k=0}^P D_{Pk} u_{ik}^{m_1, m_2} + \frac{1}{\Delta x_2^{m_2+1}} \sum_{l=0}^P D_{0l} u_{il}^{m_1, m_2+1} \\ &\quad + \mu_{\text{IP}}^{m_1, m_2+1/2} \left(u_{i0}^{m_1, m_2+1} - u_{iP}^{m_1, m_2} \right) \end{aligned} \quad (12b)$$

and for LDG

$$\begin{aligned} \hat{\sigma}_{1,j}^{m_1+1/2, m_2} &= \frac{1+2\beta_1}{\Delta x_1^{m_1}} \sum_{k=0}^P D_{Pk} u_{kj}^{m_1, m_2} + \frac{1-2\beta_1}{\Delta x_1^{m_1+1}} \sum_{l=0}^P D_{0l} u_{lj}^{m_1+1, m_2} \\ &\quad + \left[\frac{(1+2\beta_1)^2}{2\Delta x_1^{m_1}\rho_P} + \frac{(1-2\beta_1)^2}{2\Delta x_1^{m_1+1}\rho_0} + \mu_{\text{LDG}}^{m_1+1/2, m_2} \right] \left(u_{0j}^{m_1+1, m_2} - u_{Pj}^{m_1, m_2} \right), \end{aligned} \quad (13a)$$

$$\begin{aligned} \hat{\sigma}_{2,i}^{m_1, m_2+1/2} &= \frac{1+2\beta_2}{\Delta x_2^{m_2}} \sum_{k=0}^P D_{Pk} u_{ik}^{m_1, m_2} + \frac{1-2\beta_2}{\Delta x_2^{m_2+1}} \sum_{l=0}^P D_{0l} u_{il}^{m_1, m_2+1} \\ &\quad + \left[\frac{(1+2\beta_2)^2}{2\Delta x_2^{m_2}\rho_P} + \frac{(1-2\beta_2)^2}{2\Delta x_2^{m_2+1}\rho_0} + \mu_{\text{LDG}}^{m_1, m_2+1/2} \right] \left(u_{i0}^{m_1, m_2+1} - u_{iP}^{m_1, m_2} \right). \end{aligned} \quad (13b)$$

A closer inspection of Equations (11–13) shows that IP and LDG coincide if $\beta = 0$ and

$$\begin{aligned}\mu_{\text{IP}}^{m_1+1/2, m_2} &= \left(\frac{1}{2\Delta x_1^{m_1} \rho_P} + \frac{1}{2\Delta x_1^{m_1+1} \rho_0} \right) + \mu_{\text{LDG}}^{m_1+1/2, m_2} = \mu_0^{m_1+1/2, m_2} + \mu_{\text{LDG}}^{m_1+1/2, m_2}, \\ \mu_{\text{IP}}^{m_1, m_2+1/2} &= \left(\frac{1}{2\Delta x_2^{m_2} \rho_P} + \frac{1}{2\Delta x_2^{m_2+1} \rho_0} \right) + \mu_{\text{LDG}}^{m_1, m_2+1/2} = \mu_0^{m_1, m_2+1/2} + \mu_{\text{LDG}}^{m_1, m_2+1/2}.\end{aligned}$$

This observation allows to relate the interior penalty method to the LDG stability condition $\mu_{\text{LDG}} > 0$ and motivates the generic penalty coefficient

$$\mu = \mu_0 (1 + \mu_\star),$$

where $\mu_\star > 0$ is a dimensionless parameter and μ_0 the LDG stability threshold, e.g., at $\Gamma^{m_1+1/2, m_2}$

$$\mu_0^{m_1+1/2, m_2} = \frac{1}{2\Delta x_1^{m_1} \rho_P} + \frac{1}{2\Delta x_1^{m_1+1} \rho_0}.$$

The original coefficients are related to the generic one by $\mu_{\text{IP}} = \mu$ and $\mu_{\text{LDG}} = \mu_0 \mu_\star$. Introducing these definitions in (12) and (13) yields the unified numerical fluxes

$$\begin{aligned}\hat{\sigma}_{1,j}^{m_1+1/2, m_2} &= \frac{1 + 2\beta_1}{\Delta x_1^{m_1}} \sum_{k=0}^P D_{Pk} u_{kj}^{m_1, m_2} + \frac{1 - 2\beta_1}{\Delta x_1^{m_1+1}} \sum_{l=0}^P D_{0l} u_{lj}^{m_1+1, m_2} \\ &+ \left[2 \frac{\beta_1^2 + \beta_1}{\Delta x_1^{m_1} \rho_P} + 2 \frac{\beta_1^2 - \beta_1}{\Delta x_1^{m_1+1} \rho_0} + \mu^{m_1+1/2, m_2} \right] \left(u_{0j}^{m_1+1, m_2} - u_{Pj}^{m_1, m_2} \right),\end{aligned}\tag{14a}$$

$$\begin{aligned}\hat{\sigma}_{2,i}^{m_1, m_2+1/2} &= \frac{1 + 2\beta_2}{\Delta x_2^{m_2}} \sum_{k=0}^P D_{Pk} u_{ik}^{m_1, m_2} + \frac{1 - 2\beta_2}{\Delta x_2^{m_2+1}} \sum_{l=0}^P D_{0l} u_{il}^{m_1, m_2+1} \\ &+ \left[2 \frac{\beta_2^2 + \beta_2}{\Delta x_2^{m_2} \rho_P} + 2 \frac{\beta_2^2 - \beta_2}{\Delta x_2^{m_2+1} \rho_0} + \mu^{m_1, m_2+1/2} \right] \left(u_{i0}^{m_1, m_2+1} - u_{iP}^{m_1, m_2} \right).\end{aligned}\tag{14b}$$

With these prerequisites we are ready to tackle (5b). Setting $v|_{\Omega^m} = \varphi_i(\xi_1)\varphi_j(\xi_2)$, applying (4) and applying the GLL quadrature leads to the discrete equations

$$\begin{aligned}
& \Delta x_2^{m_2} \rho_j \left[\frac{1}{\Delta x_1^{m_1}} \sum_{k=0}^P L_{ik} u_{kj}^{m_1, m_2} \right. \\
& \quad + \frac{1-2\beta_1}{2\Delta x_1^{m_1}} D_{0i} (u_{0j}^{m_1, m_2} - u_{Pj}^{m_1-1, m_2}) + \frac{\delta_{i0}}{2} \hat{\sigma}_{1,j}^{m_1-1/2, m_2} \\
& \quad \left. + \frac{1+2\beta_1}{2\Delta x_1^{m_1}} D_{Pi} (u_{0j}^{m_1+1, m_2} - u_{Pj}^{m_1, m_2}) - \frac{\delta_{iP}}{2} \hat{\sigma}_{1,j}^{m_1+1/2, m_2} \right] \\
& + \Delta x_1^{m_1} \rho_i \left[\frac{1}{\Delta x_2^{m_2}} \sum_{l=0}^P L_{il} u_{il}^{m_1, m_2} \right. \\
& \quad + \frac{1-2\beta_2}{2\Delta x_2^{m_2}} D_{0j} (u_{i0}^{m_1, m_2} - u_{iP}^{m_1, m_2-1}) + \frac{\delta_{j0}}{2} \hat{\sigma}_{2,i}^{m_1, m_2-1/2} \\
& \quad \left. + \frac{1+2\beta_2}{2\Delta x_2^{m_2}} D_{Pj} (u_{i0}^{m_1, m_2+1} - u_{iP}^{m_1, m_2}) - \frac{\delta_{jP}}{2} \hat{\sigma}_{2,i}^{m_1, m_2+1/2} \right] \\
& = \frac{\Delta x_1^{m_1} \Delta x_2^{m_2}}{4} \rho_i \rho_j f(x_1^{m_1}(\eta_i), x_2^{m_2}(\eta_j)) =: g_{ij}^{m_1, m_2} \quad (15)
\end{aligned}$$

for $0 \leq i, j \leq P$ and $1 \leq m_d \leq N_{E,d}$, where $x_d^{m_d}(\xi_d)$, $d = 1, 2$, is the inverse element mapping and

$$L_{ik} = \int_{-1}^1 \varphi'_i(\xi) \varphi'_k(\xi) d\xi = \sum_{j=0}^P \rho_j D_{ji} D_{jk}$$

the one-dimensional standard stiffness matrix.

To emphasize the tensor-product structure of (15) we introduce the global solution coefficients $u_{IJ} = u_{ij}^{m_1, m_2}$, where

$$I = \ell_1(i, m_1) := i + (P+1)\tilde{m}_1 \quad (16a)$$

$$J = \ell_2(j, m_2) := j + (P+1)\tilde{m}_2 \quad (16b)$$

with periodic element indices $\tilde{m}_d = m_d + kN_{E,d}$, $k \in \mathbb{I}$, such that $1 \leq \tilde{m}_d \leq N_{E,d}$. Further, we define the generic 1D mass matrices

$$\tilde{M}_{\ell(i,m)\ell(k,m+r)}^m = \frac{\Delta x^m}{2} \rho_i \delta_{ik} \delta_{0r} \quad (17)$$

and stiffness matrices

$$\tilde{L}_{\ell(i,m)\ell(k,m+r)}^m = \begin{cases} L_{ik}^- & r = -1 \\ L_{ik}^0 & r = 0 \\ L_{ik}^+ & r = 1 \\ 0 & |r| > 1 \end{cases} \quad (18)$$

with

$$\begin{aligned}
L_{ik}^0 &= \frac{2}{\Delta x^m} L_{ik} \\
&+ \frac{1-2\beta}{\Delta x^m} D_{0i} \delta_{k0} + \frac{1-2\beta}{\Delta x^m} \delta_{i0} D_{0k} + \left[2 \frac{\beta^2 + \beta}{\Delta x^{m-1} \rho_P} + 2 \frac{\beta^2 - \beta}{\Delta x^m \rho_0} + \mu^{m-1/2} \right] \delta_{i0} \delta_{k0} \\
&- \frac{1+2\beta}{\Delta x^m} D_{Pi} \delta_{kP} - \frac{1+2\beta}{\Delta x^m} \delta_{iP} D_{Pk} + \left[2 \frac{\beta^2 + \beta}{\Delta x^m \rho_P} + 2 \frac{\beta^2 - \beta}{\Delta x^{m+1} \rho_0} + \mu^{m+1/2} \right] \delta_{iP} \delta_{kP} \\
L_{ik}^- &= -\frac{1-2\beta}{\Delta x^{m-1}} D_{0i} \delta_{kP} + \frac{1+2\beta}{\Delta x^{m-1}} \delta_{i0} D_{Pk} - \left[2 \frac{\beta^2 + \beta}{\Delta x^{m-1} \rho_P} + 2 \frac{\beta^2 - \beta}{\Delta x^m \rho_0} + \mu^{m-1/2} \right] \delta_{i0} \delta_{kP} \\
L_{ik}^+ &= \frac{1+2\beta}{\Delta x^{m+1}} D_{Pi} \delta_{k0} - \frac{1-2\beta}{\Delta x^{m+1}} \delta_{iP} D_{0k} - \left[2 \frac{\beta^2 + \beta}{\Delta x^m \rho_P} + 2 \frac{\beta^2 - \beta}{\Delta x^{m+1} \rho_0} + \mu^{m+1/2} \right] \delta_{iP} \delta_{k0} .
\end{aligned}$$

Adopting these operators for both directions allows to rewrite (15) as

$$\sum_{L=0}^{N_2} \sum_{K=0}^{N_1} \underbrace{\left(\tilde{M}_{2,JL} \tilde{L}_{1,IK} + \tilde{L}_{2,JL} \tilde{M}_{1,IK} \right)}_{A_{IJ,KL}} u_{KL} = g_{IJ} \quad (19)$$

for $0 \leq I \leq N_1 = N_P N_{E,1}$ and $0 \leq J \leq N_2 = N_P N_{E,2}$, where $N_P = P + 1$ or, equivalently, in matrix form

$$\mathbf{A} \mathbf{u} = \mathbf{M}_2 \otimes \mathbf{L}_1 + \mathbf{L}_2 \otimes \mathbf{M}_1 = \mathbf{g} . \quad (20)$$

3. SOLUTION METHODS

The linear system (20) is symmetric positive semi-definite. Moreover, its structure closely resembles the discrete equations generated with the continuous spectral element method [26, 33]. This coincidence inspired us to adopt the multigrid techniques developed in [33] for the present discontinuous formulation. In particular, we examine polynomial multigrid (MG) and multigrid-preconditioned conjugate gradients (MGCG). Both approaches employ overlapping Schwarz methods for smoothing. We first present the Schwarz methods and then sketch MG and MGCG.

3.1. Schwarz methods. Schwarz methods are iterative domain decomposition techniques which improve the approximate solution by parallel or sequential subdomain solves, leading to additive or multiplicative methods, respectively. Here we consider element-centered and face-centered subdomains as illustrated in Fig. 2. The element-centered domain was already used in [33]. It covers the element region extended by a strip including N_o layers of additional nodes from the neighbor elements, excluding the nodes located on the boundary (Fig. 2a). The overlap width with is given in standard coordinates by

$$\delta_{\xi,o} = \eta_{N_o} + 1 ,$$

where η_{N_o} is the coordinate of the corresponding GLL point. In physical space, δ_o depends on the normal extension of the overlapped element and hence, can vary even within a single domain. Except for the non-overlapping case, the use of element-centered domains

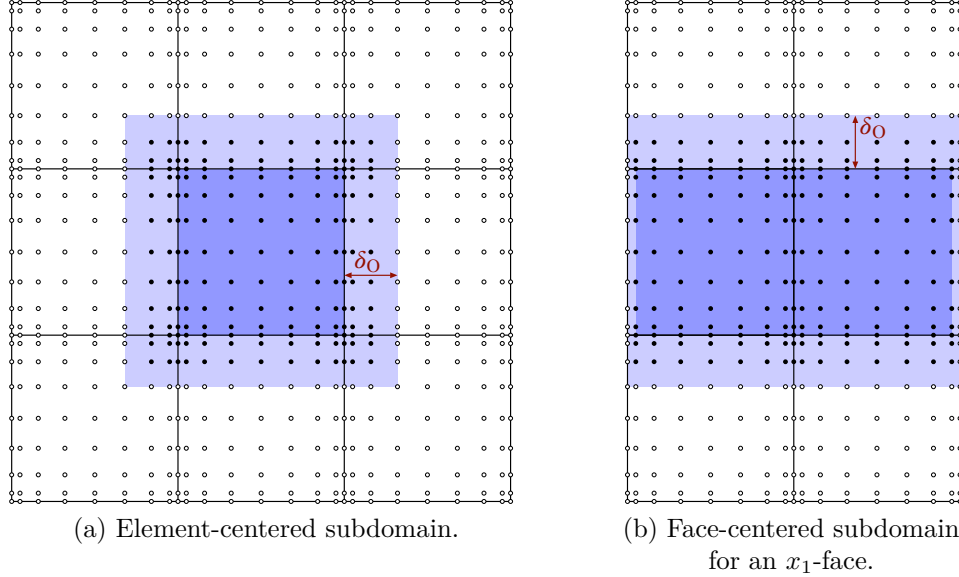


FIGURE 2. Subdomains used with the Schwarz method. Each domain consists of a core region (dark shaded) and an adjustable overlap zone of width δ_0 (light shaded). The circles are the GLL nodes for polynomial order $p = 8$. Filled circles indicate the nodes that are solved for and updated.

implies a diagonal coupling, which is natural to continuous elements, but seems artificial to DG. This motivated the use face-centered subdomains, which originally included only nodes from the two elements sharing one face (i.e. one edge in 2D). However, in course of our studies it proved necessary to allow for a lateral overlap analogous to the element-centered approach, which finally led to the face-centered domains sketched in Fig. 2b. In the normal direction the domain extends to the opposite faces, which implies a fixed overlap amounting to half the element width on each side. Contrary to the element-centered domains, the face-centered domains are oriented into either x_1 - or x_2 -direction. Consequently, we divide the face-centered domains into two groups according to their orientation. Within each group we apply lexical numbering, as is done in the element-centered case.

To derive a local correction to some approximate solution $\tilde{\mathbf{u}}$ we convert Eq. (20) into the equivalent residual form

$$\mathbf{A}\Delta\mathbf{u} = \mathbf{f} - \mathbf{A}\tilde{\mathbf{u}} = \tilde{\mathbf{r}},$$

where $\Delta\mathbf{u} = \tilde{\mathbf{u}} - \mathbf{u}$. For each subdomain Ω_s we introduce the restriction operator \mathbf{R}_s such that $\mathbf{u}_s = \mathbf{R}_s\mathbf{u}$ gives the associated coefficients. Conversely, the transposed restriction operator, \mathbf{R}_s^T is used to globalize local coefficients by adding zeros for exterior nodes. With these prerequisites the correction contributed by Ω_s is defined as the solution of the subproblem

$$\mathbf{A}_{ss}\Delta\mathbf{u}_s = \mathbf{r}_s, \quad (21)$$

where $\mathbf{A}_{ss} = \mathbf{R}_s \mathbf{A} \mathbf{R}_s^T$ represents the restricted system matrix and $\mathbf{r}_s = \mathbf{R}_s \tilde{\mathbf{r}}$ the restricted residual. Due to the rectangular shape of the subdomain, the restriction operator possesses the tensor-product factorization $\mathbf{R}_s = \mathbf{R}_{s,1} \otimes \mathbf{R}_{s,2}$ and \mathbf{A}_{ss} inherits the structure of the full system matrix \mathbf{A} , i.e.

$$\mathbf{A}_{ss} = \mathbf{M}_{s,2} \otimes \mathbf{L}_{s,1} + \mathbf{L}_{s,2} \otimes \mathbf{M}_{s,1}.$$

Note that the one-dimensional mass matrices $\mathbf{M}_{s,d} = \mathbf{R}_{s,d} \mathbf{M}_d \mathbf{R}_{s,d}^T$ are positive diagonal, while the stiffness matrices $\mathbf{L}_{s,d} = \mathbf{R}_{s,d} \mathbf{L}_d \mathbf{R}_{s,d}^T$ are symmetric and — because of the implied Dirichlet conditions — positive definite. These properties allow for application of the fast diagonalization technique (FDM) developed by Lynch et al. [27] and adopted for SEM in [8], which yields the inverse of \mathbf{A}_{ss} in the form

$$\mathbf{A}_{ss}^{-1} = (\mathbf{S}_2 \otimes \mathbf{S}_1)(\mathbf{I} \otimes \mathbf{A}_1 + \mathbf{A}_2 \otimes \mathbf{I})^{-1}(\mathbf{S}_2^T \otimes \mathbf{S}_1^T),$$

where \mathbf{I} is the unity matrix, \mathbf{S}_d an orthogonal matrix composed of the eigenvectors to the generalized eigenproblem for $\mathbf{L}_{s,d}$ and $\mathbf{M}_{s,d}$, and \mathbf{A}_d the diagonal matrix of eigenvalues. Hence, the solution $\Delta \mathbf{u}_s = \mathbf{A}_{ss}^{-1} \mathbf{r}_s$ can be evaluated with just $\Theta(C_D N_P^3)$ operations, where $C_D = 4(1 + 2C_O)^3$ for an element-centered subdomain, $C_D = 12(1 + 2C_O)(1 + 2C_O/3)$ for a face-centered subdomain, and $C_O = N_O/N_P$. Further we remark that with the former the number of domains, N_D , equals the number of elements, whereas with the latter $N_D = 2N_E$.

Several options exist for combining the local solutions. Following [33] we consider the multiplicative Schwarz method and a weighted version of the additive Schwarz method. The multiplicative Schwarz method solves the subproblems (21) consecutively, while continually updating the residual. Though \mathbf{A} is symmetric, one multiplicative Schwarz iteration corresponds to the application of a non-symmetric linear operator. However, for an even number of steps, the method is symmetrized by reversing the order of subdomains in each step.

The weighted additive Schwarz method determines all local corrections independently and computes the global correction as a linear combination of these results, i.e.

$$\Delta \mathbf{u} \simeq \sum_s \mathbf{R}_s^T (\mathbf{w} \Delta \mathbf{u}_s), \quad (22)$$

where $\mathbf{w} = \mathbf{w}_2 \otimes \mathbf{w}_1$ is a diagonal local weighting matrix that is generated from generic 1D weight distributions \mathbf{w}_d . For the element-centered approach we reuse the weight distributions introduced in [33] for the continuous case, i.e., \mathbf{w}_d is computed from the hat-shaped weighting function

$$w_H(\xi) = \frac{1}{2} \left[1 + \phi_i \left(\frac{\xi + 1}{\delta_o} \right) - \phi_i \left(\frac{\xi - 1}{\delta_o} \right) \right], \quad (23)$$

where ξ is the 1D standard coordinate extended beyond $[-1, 1]$ and ϕ_i a transitional function. Here we consider the smoothed sign functions ϕ_i with $i \in \{1, 3, 5, \dots\}$ defined as

$$\phi_i(x) = \begin{cases} \tilde{\phi}_i(x) & x \in [-1, 1] \\ \text{sgn}(x) & \text{else} \end{cases}$$

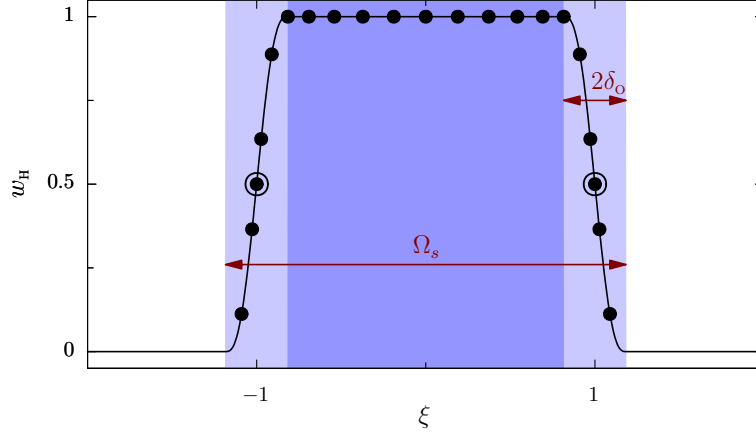


FIGURE 3. Hat-shaped weight distribution w_h for elements of order $p = 16$ with an overlap of $N_o = 3$ points using a quintic shape function. The core region and the overlap zone of the subdomain are shaded in dark and light blue, respectively. Filled circles indicate the node positions. The double valued nodes at the element boundary are indicated by a second circle.

where $\tilde{\phi}_i$ is a polynomial of degree i satisfying the conditions

$$\begin{aligned} \tilde{\phi}_i(\pm 1) &= \pm 1 \\ \frac{d^k \tilde{\phi}_i}{dx^k}(\pm 1) &= 0, \quad 0 < k \leq (i-1)/2. \end{aligned}$$

The $\tilde{\phi}_i$ are strictly monotonic in $(-1, 1)$ and yield a smooth transition of the weight function in the overlap zone. In the following we use the cubic and quintic transitions

$$\begin{aligned} \tilde{\phi}_3 &= (3x - x^3)/2, \\ \tilde{\phi}_5 &= (15x - 10x^3 + 3x^5)/8. \end{aligned}$$

Figure 3 exemplifies the resulting weight distribution for the quintic case. Other possible choices include conventional additive Schwarz, $\phi_i = 1$, and arithmetic averaging, $\tilde{\phi}_i = 0$, as proposed by Lottes and Fischer [26] for SEM.

With the face-centered approach we perform a first sweep over all subdomains of one orientation, followed by second sweep for the other orientation. Note that this method is not strictly additive, since the second sweep builds on the result of the first one. The weight matrix \mathbf{w} is constructed similarly as in the element-centered case. For the direction normal to the face we define the weighting function

$$w_F(\xi) = \frac{1}{2} [1 + \phi_i(\pm \xi)], \quad (24)$$

where the sign of ξ is chosen such that $w_F = 1$ on the face. The tangential weights are based on the hat-shaped distribution generated with (23).

3.2. Multigrid. For MG we define a series of polynomial levels $\{P_l\}$ with $P_l = 2^l$ increasing from 1 at $l = 0$ to P at top level L . Correspondingly, let \mathbf{u}_l denote the global coefficients and \mathbf{A}_l the system matrix on level l . On the top level we have $\mathbf{u}_L = \mathbf{u}$ and $\mathbf{A}_L = \mathbf{A}$, whereas on lower levels \mathbf{u}_l is the defect correction and \mathbf{A}_l the counterpart of \mathbf{A} obtained with elements of order P_l . For transferring the correction from level $l - 1$ to level l we use the embedded interpolation operator \mathcal{I}_l , and for restricting the residual its transpose. These ingredients allow to build a multigrid V-cycle, which is identical to the continuous case [33], but repeated for convenience in Algorithm 1. The SMOOTHER is designed as a generic procedure which employs either the multiplicative or the weighted additive Schwarz method with element-centered or face-centered subdomains. To allow for variable V cycles [4], the number of pre- and post-smoothing steps, $N_{s1,l}$ and $N_{s2,l}$, may change from level to level. Line 8 of Algorithm 1 defines the coarse grid solution by means of the pseudoinverse \mathbf{A}_0^+ . In our implementation the coarse problem is solved using the conjugate gradient method. To ensure convergence in spite of singularity, the right side is projected to the null space of \mathbf{A}_0 , as advocated by Kaasschieter [21].

Algorithm 1 Multigrid V-cycle.

```

1: function MULTIGRIDCYCLE( $\mathbf{u}, \mathbf{f}, \mathbf{N}_s$ )
2:    $\mathbf{u}_L \leftarrow \mathbf{u}$ 
3:    $\mathbf{f}_L \leftarrow \mathbf{f}$ 
4:   for  $l = L, 1$  step  $-1$  do
5:      $\mathbf{u}_l \leftarrow \text{SMOOTHER}(\mathbf{u}_l, \mathbf{f}_l, N_{s1,l})$  ▷ Pre-smoothing
6:      $\mathbf{f}_{l-1} \leftarrow \mathcal{I}_l^T(\mathbf{f}_l - \mathbf{A}_l \mathbf{u}_l)$  ▷ Residual restriction
7:   end for
8:    $\mathbf{u}_0 \leftarrow \mathbf{A}_0^+ \mathbf{f}_0$  ▷ Coarse grid solution
9:   for  $l = 1, L$  do
10:     $\mathbf{u}_l \leftarrow \mathbf{u}_l + \mathcal{I}_l \mathbf{u}_{l-1}$  ▷ Correction prolongation
11:     $\mathbf{u}_l \leftarrow \text{SMOOTHER}(\mathbf{u}_l, \mathbf{f}_l, N_{s2,l})$  ▷ Post-smoothing
12:  end for
13:  return  $\mathbf{u} \leftarrow \mathbf{u}_L$ 
14: end function

```

3.3. Preconditioned conjugate gradients. Robustness and efficiency of multigrid can be enhanced by Krylov acceleration [34]. Here we follow the strategy devised [33], where the inexact preconditioned conjugate gradients of Golub and Ye [14] was adopted to cope with the (slight) asymmetry introduced by the Schwarz method. The resulting MGCG method is summarized in Algorithm 2. Note that, as before with the coarse problem, the right side \mathbf{f} must be in the null space of \mathbf{A} if the system is singular.

4. RESULTS

For assessing robustness and efficiency, the described methods were implemented in Fortran and applied to the test case of Lottes and Fischer [12, 26]. The the source was $f = 2\pi^2 \sin(\pi x) \sin(\pi y)$ and the initial guess was chosen at random with values confined

Algorithm 2 Inexact multigrid preconditioned conjugate gradients.

```

1: function MGCG( $\mathbf{u}, \mathbf{f}, \mathbf{N}_s, i_{\max}, r_{\max}$ )
2:    $\mathbf{r}_{\text{old}} \leftarrow \mathbf{0}$ 
3:    $\mathbf{r} \leftarrow \mathbf{f} - \mathbf{A}\mathbf{u}$ 
4:    $\mathbf{p} \leftarrow \text{MULTIGRIDCYCLE}(\mathbf{0}, \mathbf{r}, \mathbf{N}_s)$ 
5:    $\delta \leftarrow \mathbf{p}^T \mathbf{r}$ 
6:   for  $i = 1, i_{\max}$  do
7:      $\mathbf{q} \leftarrow \mathbf{A}\mathbf{p}$ 
8:      $\alpha \leftarrow \delta / (\mathbf{p}^T \mathbf{q})$ 
9:      $\mathbf{u} \leftarrow \mathbf{u} + \alpha \mathbf{p}$ 
10:     $\mathbf{r} \leftarrow \mathbf{r} - \alpha \mathbf{q}$ 
11:    if  $\|\mathbf{r}\| \leq r_{\max}$  exit
12:     $\mathbf{z} \leftarrow \text{MULTIGRIDCYCLE}(\mathbf{0}, \mathbf{r}, \mathbf{N}_s)$ 
13:     $\beta \leftarrow \mathbf{q}^T (\mathbf{r} - \mathbf{r}_{\text{old}}) / \delta$ 
14:     $\mathbf{p} \leftarrow \mathbf{z} + \beta \mathbf{p}$ 
15:     $\delta \leftarrow \mathbf{z}^T \mathbf{r}$ 
16:     $\mathbf{r}_{\text{old}} \leftarrow \mathbf{r}$ 
17:  end for
18:  return  $\mathbf{u}$ 
19: end function

```

to the interval $[0, 1]$. To keep the test series manageable, we constrained ourselves to equidistant grids, but varied the aspect ratio $AR = \Delta x_1 / \Delta x_2$. The code was compiled using the GNU compiler collection 6.0 with optimization -O3 and run on a 3.1 GHz Intel Core i7-5557U CPU.

4.1. Performance metrics. The primary convergence measure is the average multigrid convergence rate

$$\rho = \sqrt[n]{\frac{r_n}{r_0}},$$

where r_n is the Euclidean norm of the residual vector after the n th cycle. Since ρ varied by several orders of magnitude in some tests, we use alternatively the logarithmic convergence rate

$$\bar{r} = -\log_{10} \rho$$

and the number of cycles n_{10} needed to reduce the residual by a factor of 10^{10} .

As an efficiency measure we define the equivalent number of operator applications required for reducing the residual by a factor of 10^k ,

$$\bar{\omega}_k = \frac{k}{\bar{r}} \frac{W_{\text{cyc}}}{W_{\text{op}}},$$

where W_{op} is the cost for one application of the system matrix \mathbf{A} and W_{cyc} for one cycle. Assuming that sum factorization is exploited, the former can be estimated as $W_{\text{op}} = 2N_{\text{P}}^3 N_{\text{E}}$. The cycle cost comprises the contributions of Schwarz iterations, residual

evaluations, the coarse grid solver and transfer operators. Using the estimates given in Sec. 3.1 for the first and neglecting the latter two we arrive at

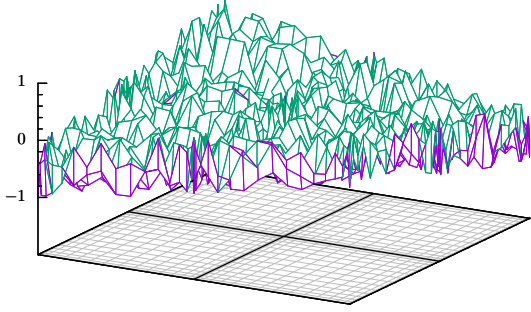
$$W_{\text{cyc}} \simeq \left[C_s N_s \left(\frac{C_D}{2} \frac{N_D}{N_E} + 1 \right) + C_{\text{CG}} \right] W_{\text{op}},$$

where N_s is the number of pre- and post-smoothing steps on the finest level, $C_s = 4/3$ for the classical V-cycle and 2 for a variable V-cycle doubling the number of smoothing steps with lower levels [4], and $C_{\text{CG}} = 1$ the extra cost for conjugate gradients when using MGCG. The “1” in the inner braces stems from the residual evaluation, which is also the dominant cost with CG.

4.2. Qualitative behavior of Schwarz methods. Figure 4 illustrates the smoothing properties of selected additive Schwarz methods for a discretization using 8×8 elements of order $P = 16$ with stabilization $\mu_\star = 1$ and auxiliary parameter $\beta = 0$. The displayed error is defined as the difference between the approximate and exact solutions adjusted to a zero median. For clarity, the plots were restricted to a subregion comprising four elements. Figure 4a depicts the error of the random initial guess and Figs. 4b-f the error after one iteration with different Schwarz methods. In particular, Fig. 4b and Fig. 4c reveal that the non-overlapping element-centered method and the unweighted element-centered method with overlap $N_o = 3$ fail to smooth the error across the element boundaries. The jumps produced with both methods tend to dominate the residual and lead to a severe degradation of MG efficiency. Arithmetically weighting the overlapping Schwarz updates greatly improves this behavior, although the error still exhibits ridges near the element boundaries (Fig. 4d). Using a smooth hat-shaped weight distribution removes these ridges and yields the best smoothing properties for element-centered subdomains (Fig. 4e). Finally, Figure 4f illustrates the excellent performance of the overlapping face-centered Schwarz method with cubic weighting. It should be noted, however, that one face-centered iteration has two sweeps instead of one with element-centered domains and, in addition to this, employs a larger overlap into the face normal direction.

4.3. Convergence and robustness. To investigate the influence of overlap and weighting, and to assess the robustness of the multigrid approach we performed several numerical experiments on triangulations consisting of up to 256^2 elements of order $P = 4$ to 32 and aspect ratios between 1 and 32. For concise notation we use two-letter acronyms, where the first letter identifies the subdomain type (“E” – element-centered, “F” – face-centered) and the second the iteration method (“M” – multiplicative, “A” additive). Additionally, subscript “0” indicates zero overlap, $N_o = 0$, and “ ℓ ” a level-dependent overlap of $N_{o,\ell} = 1 + \lfloor P_\ell/8 \rfloor$. For example, FM_0 denotes the face-centered multiplicative Schwarz method with $N_o = 0$, i.e. no lateral overlap. If not indicated otherwise, one pre-smoothing and one post-smoothing step were applied on each level $l > 0$. The weighting method (cubic or quintic) is stated where necessary.

Table 2 shows the convergence rates of selected MG and MGCG methods on a uniform 16×16 tessellation of the domain $[0, 2]^2$. The results for the element-centered smoothers resemble those obtained with continuous spectral elements [33]. Using the multiplicative smoother with no overlap, EM_0 , MG and MGCG reach convergence rates up to $\bar{r} = 0.9$



(a) Initial error.

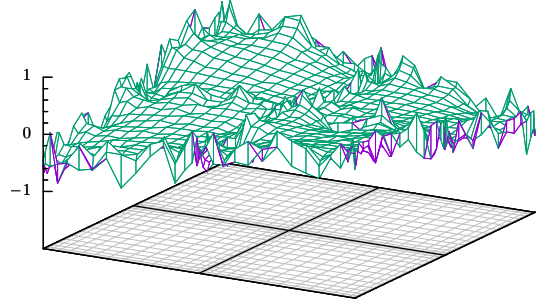
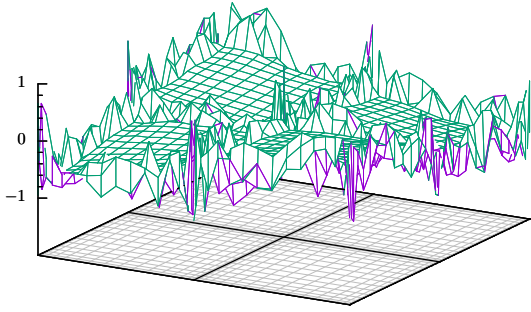
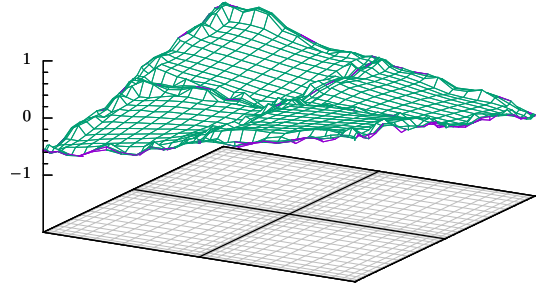
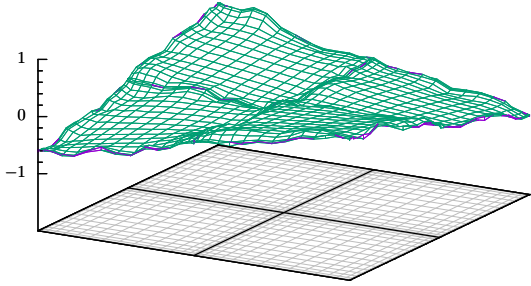
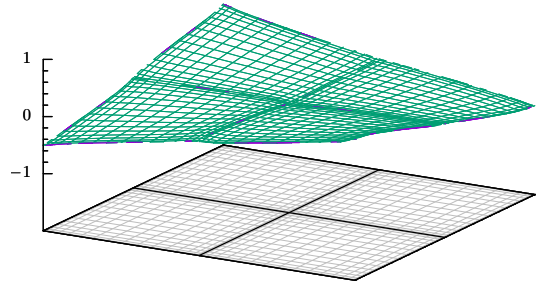
(b) Element-centered additive, $N_o = 0$.(c) Element-centered additive,
 $N_o = 3$, unweighted(d) Element-centered additive,
 $N_o = 3$, arithmetic averaging.(e) Element-centered additive,
 $N_o = 3$, cubic weighting.(f) Face-centered additive, $N_o = 3$,
cubic weighting.

FIGURE 4. Smoothing properties of selected Schwarz methods. DG with 8×8 elements of order $P = 16$, $\mu_\star = 1$ and $\beta = 0$. Graph (a) shows the initial error in a subregion consisting of four elements, and (d–f) the error after one Schwarz iteration.

with $P = 4$, but degrade with growing polynomial order P . In the additive case, EA_0 , MG fails to converge (not shown), whereas MGCG just succeeds. Lines 7–14 show the results obtained with the level-dependent overlap, $N_{o,l} = 1 + \lfloor P_l/8 \rfloor$. It imposes a lower bound on the overlap width δ_o that corresponds approximately to one eighth of the neighbor element width in the direction normal to the boundary. With this choice MG becomes robust against increasing P for multiplicative as well as additive Schwarz smoothing. Comparing the smoothers reveals that EA_ℓ consistently achieved a higher convergence rates than EM_ℓ . As a possible reason we found that the instantaneous updates in the multiplicative method tend to produce excessive gradients in overlap regions, whereas the additive method avoids this peculiarity by applying a weighted average. Both, cubic as well as quintic weighting are suited, though the latter proved slightly more efficient.

Lines 15–28 of Tab. 2 show the results for the face-centered smoothers. Compared to the element-centered smoothers, they achieve notably higher convergence rates, which can be attributed to the inbuilt overlap normal to the face and the double sweep over both coordinate directions. Even with no lateral overlap the approach proved robust against P . Application of a level-dependent lateral overlap, $N_{o,l} = 1 + \lfloor P_l/8 \rfloor$, increased the logarithmic convergence rate to magnitudes in the range between 2 and 3.5. In contrast to the element-centered method, the difference between cubic and quintic weighting is marginal and hence not considered here. Moreover, the face-centered method exhibits a lower sensitivity with respect to the auxiliary LDG parameter $\vec{\beta}$. In most cases, similar convergence rates were obtained for central and non-central numerical fluxes, i.e. $\vec{\beta} = 0$ and $\vec{\beta} = 1/2$, whereas the latter tends to converge slower than the former when using element-centered smoothers.

In the following we focus our attention to MGCG for IP/LDG with central numerical fluxes and abandon cubic in favor of quintic weighting. Table 3 shows the logarithmic convergence rates \bar{r} , cycle counts n_{10} and equivalent operator applications $\bar{\omega}_1$ for smoothers EM_0 , EA_ℓ , FA_0 and FA_ℓ on equidistant triangulations ranging from 8^2 to 256^2 elements and polynomial orders from $P = 4$ to 32. The results clearly confirm that the methods are robust with respect to the grid size. As expected, EM_0 degrades for growing P , whereas with EA_ℓ , FA_0 and FA_ℓ the increased order leads to even higher convergence rates and, hence, lower cycle counts. Comparing the average number of operator applications required for reducing the residual by a factor of 10, we find that EA_ℓ is the most efficient method with $\bar{\omega}_1 \in [6, 11]$. For example, with order $P = 16$, just 2600 multiplications per unknown yield a reduction by ten orders of magnitude. Due to the low iteration cost EM_0 remains competitive with EA_ℓ for $P = 4$ and is still the second-best method for $P = 8$. FA_ℓ converges about 1.4 times faster than EA_ℓ , but fails to compensate the sixfold higher operation count and thus remains about twice as expensive in terms of $\bar{\omega}_1$.

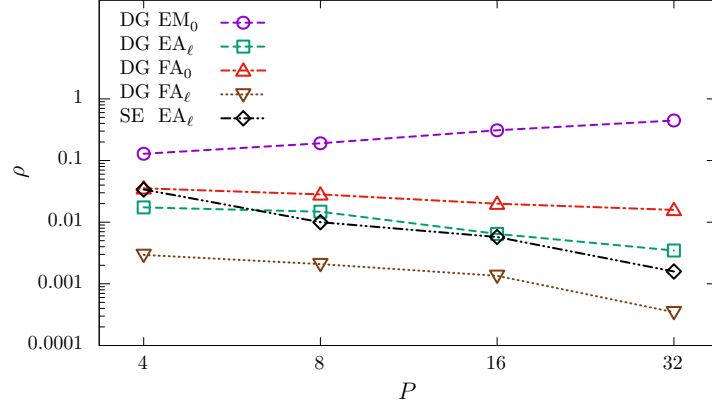
Figure 5a shows the multigrid convergence rates in comparison with the spectral element (SE) version of EA_ℓ . In line with our expectations the comparison asserts that the discontinuous and continuous methods converge nearly with identical rates, improving from $\rho \approx 0.02$ at $P = 4$ to 0.003 at $P = 32$. The face-centered additive smoother yields even faster convergence with rates between 0.003 and 0.0003. To assess the actual computational cost, Figure 5b depicts the runtimes required to reduce the residual by ten

orders of magnitude for different polynomial degrees. Note that the number of elements was adjusted according to $N_{e,d} = 256/P$ to assure a nearly constant problem size. Sum factorization was exploited on levels $P_l \geq 8$. Independent of the method, all graphs exhibit a gentle downward slope which becomes increasingly horizontal with growing P . This indicates that the increased operation count scaling as $\bar{\omega}_1 P$ is more than compensated by the gain in computational efficiency due to the larger operator size. For the same reason, the face-centered methods, FA_0 and FA_ℓ come considerably closer to EA_ℓ than predicted by $\bar{\omega}_1$. In contrast, EA_0 performs much worse than expected, consuming more than 10 times the runtime of EA_ℓ . This behavior is a consequence of the recursive solution strategy of multiplicative Schwarz: It prevents the “stacking” of operands as in the additive case, where it allows to convert matrix-vector multiplications into vastly more efficient matrix-matrix multiplications. The fastest discontinuous method, MGCG with EA_ℓ , solves the problem with $P = 16$ in 0.112 s or, respectively, $1.5 \mu\text{s}$ per unknown. Counting only multiplications, this corresponds to a performance of 1.9 GFLOPS. The spectral element counterpart attains nearly identical convergence rates, but succeeds with just two thirds of the runtime, which corresponds almost exactly to the lower operation count.

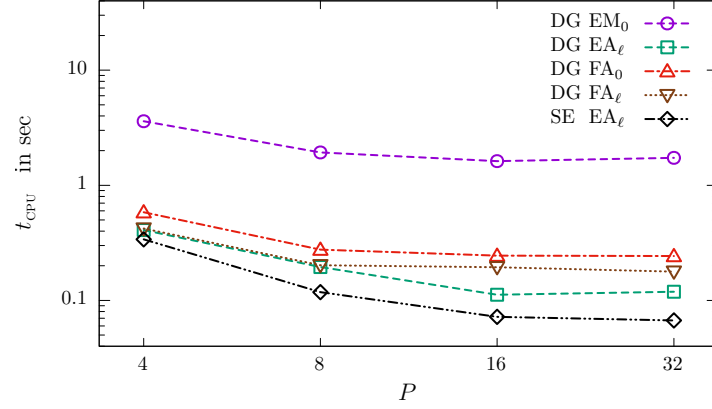
For assessing the sensitivity to the element aspect ratio, $AR = \Delta x_1/\Delta x_2$, we defined a series of rectangular domains $\Omega = [0, 2] \times [0, 2AR]$ with AR varying from 1 to 32. Each domain is decomposed into 16×16 rectangular elements of the order P , which ranged from 4 to 32. In addition to the methods considered above, the tests included variants using a variable V-cycle. With the latter the number of smoothing steps is doubled when switching to the next coarser level, i.e. $N_{s,l} = (2^{L-l}, 2^{L-l})$. The variable V-cycle improves convergence speed and robustness, but also raises the cost of one cycle by approximately 50%. In our tests we observed runtime savings in face-centered case, whereas the extra cost prevailed in the element-centered case. According to Tab. 4, both element-centered methods show a strong sensitivity to the aspect ratio: EM_0 degrades severely as soon as AR exceeds 4, whereas EA_ℓ retains still 30 to 40 percent of the original convergence rate with $AR = 8$. In comparison, the face-centered methods proved rather robust, in particular with higher ansatz order. For example, with FA_0 , n_{10} multiplies by 5 when increasing AR from 1 to 16 for $P = 4$, but only by 1.4 for $P = 16$. The overlapping face-centered method, FA_ℓ exhibits a similar behavior. Finally, Figure 6 shows the corresponding runtimes for $P = 16$. EA_ℓ remains the fastest method for $AR \leq 2$, whereas EA_0 is by far the slowest. Due to their better robustness, FA_ℓ and FA_0 close up with growing aspect ratio. They break even with EA_ℓ at $AR = 4$ and $AR = 8$, respectively, and gain a clear advantage for higher aspect ratios.

5. CONCLUSIONS

We presented a multigrid method for nodal discontinuous Galerkin formulations of the Poisson equation on two-dimensional Cartesian grids. The method adopts and extends techniques developed recently for the continuous spectral element method [26, 33]. Using the nodal basis corresponding to the Gauss-Lobatto-Legendre points in conjunction with the related quadrature we derived a unified form of the discrete equations, which embodies



(a) Convergence rates.



(b) Runtimes.

FIGURE 5. MGCG convergence rates and runtimes for a 10^{10} residual reduction using $(256/P)^2$ square elements of order P . DG denotes the discontinuous Galerkin method with parameters and smoothers according to Tab. 3, and SE the corresponding spectral element method.

the interior penalty method as well as the local discontinuous Galerkin method. These equations are solved by means of polynomial multigrid with multiplicative or weighted additive Schwarz methods for smoothing and, optionally, the inexact preconditioned conjugate gradient method [14] for acceleration. The Schwarz methods operate on a set of overlapping rectangular subdomains, which are either element- or face-centered. The resulting multigrid methods achieved excellent convergence rates independent from the problem size. Using a level-dependent overlap of $1 + \lfloor P_l/8 \rfloor$ nodes proved sufficient for robustness against the ansatz order up to $P = 32$. Taking advantage of tensor-product factorization and fast diagonalization techniques, the methods attain a computational complexity of $O(PN)$ per cycle. In terms of runtime, the solvers actually achieve linear

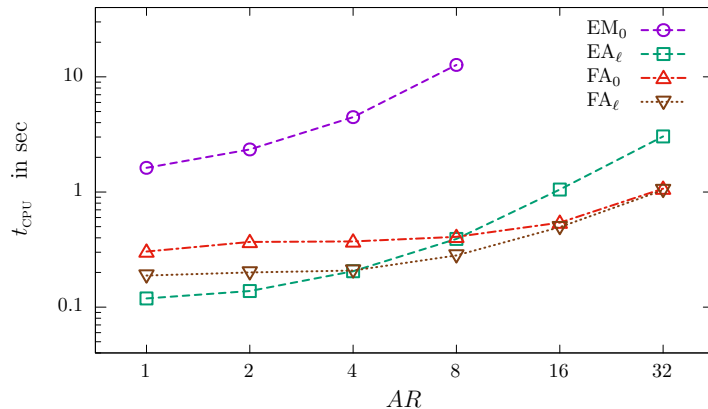


FIGURE 6. MGCG runtimes for a 10^{10} residual reduction at different aspect ratios. Discretization using 16×16 elements of order $P=16$ with 73,984 unknowns; parameters and smoothers as in Tab. 4.

complexity, since the convergence rate and the computational efficiency improve with growing order. MGCG with EA_ℓ is the best choice for equidistant triangulations with nearly quadratic elements, for which it achieves convergence rates between $\rho = 0.017$ and 0.003 . With $P = 16$ it needs about 2600 multiplications per unknown to reduce the residual by ten orders of magnitudes. MGCG with FA_ℓ is twice as costly under these conditions, but proves more robust against the aspect ratio and becomes the preferred choice for $AR > 4$.

The proposed multigrid methods present an opportunity to enhance the competitiveness of high-order discontinuous Galerkin methods in more complex applications such as computational fluid dynamics. Due to its tensor-product structure, the approach offers a straightforward extension to three-dimensional problems, which is the subject to ongoing work. Further challenges include the development of multigrid preconditioners for variable diffusion and deformed meshes, as demonstrated by Fischer and Lottes [13] for the spectral element case.

REFERENCES

- [1] P. F. Antonietti, M. Sarti, and M. Verani. Multigrid algorithms for hp -discontinuous Galerkin discretizations of elliptic problems. *SIAM Journal on Numerical Analysis*, 53(1):598–618, 2015.
- [2] D. N. Arnold, F. Brezzi, B. Cockburn, and L. D. Marini. Unified analysis of discontinuous Galerkin methods for elliptic problems. *SIAM Journal on Numerical Analysis*, 39(5):1749–1779, 2001.
- [3] P. Bastian, M. Blatt, and R. Scheichl. Algebraic multigrid for discontinuous Galerkin discretizations of heterogeneous elliptic problems. *Numer. Linear Algebra Appl.*, 19(2):367–388, 2012.
- [4] J. Bramble. *Multigrid methods*. Pitman Res. Notes Math. Ser. 294. Longman Scientific & Technical, Harlow, UK, 1995.

- [5] B. Cockburn and C.-W. Shu. The local discontinuous Galerkin method for time-dependent convection-diffusion systems. *SIAM Journal on Numerical Analysis*, 35(6):2440–2463, 1998.
- [6] B. Cockburn, G. E. Karniadakis, and C.-W. Shu. *Discontinuous Galerkin Methods: Theory, Computation and Applications*. Springer Berlin Heidelberg, 2000.
- [7] B. Cockburn, G. Kanschat, I. Perugia, and D. Schötzau. Superconvergence of the local discontinuous Galerkin method for elliptic problems on Cartesian grids. *SIAM Journal on Numerical Analysis*, 39(1):264–285, 2002.
- [8] W. Couzy and M. O. Deville. A fast Schur complement method for the spectral element discretization of the incompressible Navier-Stokes equations. *J. Comput. Phys.*, 116:135–142, January 1995.
- [9] M. O. Deville, P. F. Fischer, and E. H. Mund. *High-Order Methods for Incompressible Fluid Flow*, volume 1. Cambridge University Press, 2002.
- [10] V. A. Dobrev, R. D. Lazarov, P. S. Vassilevski, and L. T. Zikatanov. Two-level preconditioning of discontinuous Galerkin approximations of second-order elliptic equations. *Numerical Linear Algebra with Applications*, 13(9):753–770, 2006.
- [11] K. J. Fidkowski, T. A. Oliver, J. Lu, and D. L. Darmofal. p -multigrid solution of high-order discontinuous Galerkin discretizations of the compressible Navier-Stokes equations. *Journal of Computational Physics*, 207(1):92–113, 2005.
- [12] P. F. Fischer. Personal communication, September 2015.
- [13] P. F. Fischer and J. W. Lottes. Hybrid Schwarz-multigrid methods for the spectral element method: Extensions to Navier-Stokes. In *Domain Decomposition Methods in Science and Engineering Series*, pages 35–49. Springer, 2004.
- [14] G. H. Golub and Q. Ye. Inexact preconditioned conjugate gradient method with inner-outer iteration. *SIAM Journal on Scientific Computing*, 21(4):1305–1320, Dec. 1999. ISSN 10648275.
- [15] J. Gopalakrishnan and G. Kanschat. A multilevel discontinuous Galerkin method. *Numerische Mathematik*, 95(3):527–550, 2003.
- [16] L. Haupt, J. Stiller, and W. Nagel. A fast spectral element solver combining static condensation and multigrid techniques. *J. Comput. Phys.*, 255:384–395, 2013.
- [17] B. T. Helenbrook and H. L. Atkins. Application of p -multigrid to discontinuous Galerkin formulations of the poisson equation. *AIAA Journal*, 44(3):566–575, 2006.
- [18] B. T. Helenbrook, H. L. Atkins, and D. J. Mavriplis. Analysis of p -multigrid for continuous and discontinuous finite element discretizations. AIAA Paper 2003-3989, AIAA, June 2003.
- [19] J. S. Hesthaven and T. Warburton. *Nodal Discontinuous Galerkin Methods*. Springer, 2008.
- [20] I. Huismann, J. Stiller, and J. Fröhlich. Factorizing the factorization - a spectral-element solver for elliptic equations with linear operation count. *J. Computational Physics*, 2016. (submitted).
- [21] E. F. Kaasschieter. Preconditioned conjugate gradients for solving singular systems. *J. Comput. Appl. Math.*, 24:265–275, 1988.

- [22] G. Kanschat. Multilevel methods for discontinuous Galerkin FEM on locally refined meshes. *Computers and Structures*, 82:2437–2445, 2004.
- [23] G. Kanschat. Robust smoothers for high-order discontinuous Galerkin discretizations of advection-diffusion problems. *Journal of Computational and Applied Mathematics*, 218(1):53–60, 2008.
- [24] G. E. Karniadakis and S. J. Sherwin. *Spectral/hp Element Methods for Computational Fluid Dynamics*. Oxford University Press, 2nd edition, 2005.
- [25] J. K. Kraus and S. K. Tomar. A multilevel method for discontinuous Galerkin approximation of three-dimensional anisotropic elliptic problems. *Numer. Linear Algebra Appl.*, 15(5):417–438, 2008.
- [26] J. W. Lottes and P. F. Fischer. Hybrid multigrid/Schwarz algorithms for the spectral element method. *J. Sci. Comput.*, 24:45–78, 2005.
- [27] R. E. Lynch, J. R. Rice, and D. H. Thomas. Direct solution of partial difference equations by tensor product methods. *Numer. Math.*, 6:185–199, 1964.
- [28] L. N. Olson and J. B. Schroder. Smoothed aggregation multigrid solvers for high-order discontinuous Galerkin methods for elliptic problems. *Journal of Computational Physics*, 230(18):6959–6976, 2011.
- [29] F. Prill, M. Lukáčová-Medvidová, and R. Hartmann. Smoothed aggregation multigrid for the discontinuous Galerkin method. *SIAM J. Sci. Comput.*, 31(5):3503–3528, 2009.
- [30] B. Rivière. *Discontinuous Galerkin Methods for Solving Elliptic and Parabolic Equations: Theory and Implementation*, volume 35 of *Frontiers in Mathematics*. SIAM, Philadelphia, PA, USA, 2008.
- [31] K. Shahbazi, D. J. Mavriplis, and N. K. Burgess. Multigrid algorithms for high-order discontinuous Galerkin discretizations of the compressible Navier–Stokes equations. *Journal of Computational Physics*, 228(21):7917–7940, 2009.
- [32] C. Siefert, R. Tuminaro, A. Gerstenberger, G. Scovazzi, and S. S. Collis. Algebraic multigrid techniques for discontinuous Galerkin methods with varying polynomial order. *Computational Geosciences*, 18(5):597–612, 2014.
- [33] J. Stiller. Nonuniformly weighted schwarz smoothers for spectral element multigrid. *J. Sci. Comput.*, 2016. (submitted).
- [34] U. Trottenberg, C. W. Oosterlee, and A. Schüller. *Multigrid*. Academic Press, 2000.
- [35] J. J. W. van der Vegt and S. Rhebergen. Hp-multigrid as smoother algorithm for higher order discontinuous Galerkin discretizations of advection dominated flows. Part II: Optimization of the Runge-Kutta smoother. *J. Comput. Phys.*, 231(22):7564–7583, 2012.

TABLE 2. Convergence rates of MG and MGCG with different overlaps and weighting methods. DG with $\mu_\star = 1$ and constant $\vec{\beta}$ using a uniform 16×16 triangulation.

#	method	smoother	weighting	$\vec{\beta}$	\bar{r}			
					$P=4$	$P=8$	$P=16$	$P=32$
1	MG	EM_0	—	0	0.63	0.36	0.22	0.15
2			—	$\frac{1}{2}$	0.43	0.26	0.17	0.13
3	MGCG	EM_0	—	0	0.90	0.72	0.52	0.36
4			—	$\frac{1}{2}$	0.73	0.58	0.40	0.28
5		EA_0	—	0	0.20	0.09	0.03	0.01
6			—	$\frac{1}{2}$	0.16	0.06	0.02	0.01
7	MG	EM_ℓ	—	0	1.02	1.01	1.13	1.45
8			—	$\frac{1}{2}$	0.61	0.84	0.92	1.16
9		EA_ℓ	cubic	0	1.39	1.64	1.82	1.99
10			cubic	$\frac{1}{2}$	1.52	1.69	1.70	1.98
11			quintic	0	1.66	1.65	2.11	2.51
12			quintic	$\frac{1}{2}$	1.56	1.68	2.04	2.49
13	MGCG	EA_ℓ	quintic	0	1.76	1.84	2.20	2.49
14			quintic	$\frac{1}{2}$	1.60	1.74	2.07	2.40
15	MG	FM_0	—	0	1.64	1.71	1.87	1.96
16			—	$\frac{1}{2}$	1.45	1.34	1.32	1.34
17		FA_0	quintic	0	1.15	1.22	1.32	1.37
18			quintic	$\frac{1}{2}$	1.20	1.14	1.13	1.16
19	MGCG	FM_0	—	0	1.93	2.03	2.28	2.41
20			—	$\frac{1}{2}$	1.65	1.66	1.72	1.84
21		FA_0	quintic	0	1.45	1.57	1.70	1.82
22			quintic	$\frac{1}{2}$	1.43	1.54	1.61	1.67
23	MG	FM_ℓ	—	0	2.41	2.53	2.66	2.83
24			—	$\frac{1}{2}$	2.10	2.54	3.01	3.18
25		FA_ℓ	quintic	0	2.02	2.35	2.56	3.11
26			quintic	$\frac{1}{2}$	2.47	2.61	3.26	3.53
27	MGCG	FA_ℓ	quintic	0	2.54	2.71	3.10	3.50
28			quintic	$\frac{1}{2}$	2.51	2.62	3.19	3.30

TABLE 3. Robustness of MGCG against the problem size; $\mu_\star = 1$, $\vec{\beta} = 0$, triangulation with $N_{\text{E},d} \times N_{\text{E},d}$ square elements.

P	$N_{\text{E},d}$	EM_0			EA_ℓ			FA_0			FA_ℓ		
		\bar{r}	n_{10}	$\bar{\omega}_1$	\bar{r}	n_{10}	$\bar{\omega}_1$	\bar{r}	n_{10}	$\bar{\omega}_1$	\bar{r}	n_{10}	$\bar{\omega}_1$
4	8	0.92	11	9.8	1.78	6	10.3	1.45	7	24.6	2.53	4	21.5
	16	0.90	12	10.0	1.76	6	10.4	1.45	7	24.6	2.54	4	21.4
	32	0.89	12	10.1	1.76	6	10.4	1.45	7	24.6	2.53	4	21.5
	64	0.89	12	10.1	1.76	6	10.4	1.45	7	24.6	2.53	4	21.5
	128	0.89	12	10.1	1.76	6	10.4	1.45	7	24.6	2.54	4	21.4
	256	0.89	12	10.1	1.76	6	10.4	1.45	7	24.6	2.53	4	21.5
8	8	0.73	14	12.3	1.85	6	10.7	1.55	7	23.0	2.61	4	21.7
	16	0.72	14	12.5	1.84	6	10.7	1.57	7	22.7	2.71	4	20.9
	32	0.72	14	12.5	1.84	6	10.7	1.57	7	22.7	2.63	4	21.6
	64	0.72	14	12.5	1.84	6	10.7	1.57	7	22.7	2.68	4	21.2
	128	0.72	14	12.5	1.84	6	10.7	1.57	7	22.7	2.68	4	21.2
	256	0.72	14	12.5	1.84	6	10.7	1.57	7	22.7	2.68	4	21.2
16	8	0.52	20	17.3	2.26	5	7.5	1.67	6	21.4	3.15	4	16.5
	16	0.52	20	17.3	2.20	5	7.7	1.70	6	21.0	3.10	4	16.8
	32	0.52	20	17.3	2.19	5	7.7	1.70	6	21.0	3.17	4	16.4
	64	0.52	20	17.3	2.19	5	7.7	1.70	6	21.0	3.11	4	16.7
	128	0.52	20	17.3	2.19	5	7.7	1.70	6	21.0	3.11	4	16.7
	256	0.52	20	17.3	2.19	5	7.7	1.70	6	21.0	3.12	4	16.7
32	8	0.36	28	25.0	2.46	5	6.3	1.77	6	20.2	3.47	3	14.3
	16	0.36	29	25.0	2.49	5	6.2	1.82	6	19.6	3.50	3	14.2
	32	0.36	28	25.0	2.47	5	6.3	1.82	6	19.6	3.46	3	14.3
	64	0.36	28	25.0	2.46	5	6.3	1.82	6	19.6	3.38	3	14.7
	128	0.36	28	25.0	2.46	5	6.3	1.82	6	19.6	3.52	3	14.1
	256	0.36	28	25.0	2.46	5	6.3	1.82	6	19.6	3.53	3	14.0

TABLE 4. Robustness of MGCG against the aspect ratio $AR = \Delta x_1/\Delta x_2$; $\mu_\star = 1$, $\vec{\beta} = 0$; EM₀, EA_ℓ using one pre- and one post-smoothing and FA₀, FA_ℓ a variable V-cycle with $N_{s,l} = (2^{L-l}, 2^{L-l})$.

P	AR	EM ₀		EA _ℓ		FA ₀		FA _ℓ	
		\bar{r}	n_{10}	\bar{r}	n_{10}	\bar{r}	n_{10}	\bar{r}	n_{10}
4	1	0.90	12	1.76	6	1.52	7	2.78	4
	2	0.74	14	1.26	8	1.33	8	2.49	5
	4	0.32	32	0.88	12	1.18	9	1.86	6
	8	0.13	80	0.47	22	0.85	12	1.05	10
	16	0.08	120	0.04	236	0.30	34	0.41	25
	32	0.07	140	0.03	321	0.13	79	0.16	62
8	1	0.72	14	1.84	6	1.63	7	3.10	4
	2	0.56	18	1.76	6	1.49	7	3.38	3
	4	0.29	35	1.20	9	1.43	7	2.63	4
	8	0.12	87	0.70	15	1.18	9	1.57	7
	16	0.07	141	0.25	40	0.77	14	0.91	12
	32	0.06	178	0.10	98	0.30	34	0.36	28
16	1	0.52	20	2.20	5	1.78	6	3.63	3
	2	0.37	28	2.07	5	1.62	7	3.64	3
	4	0.21	48	1.43	7	1.58	7	3.33	3
	8	0.10	97	0.85	12	1.57	7	2.58	4
	16	0.07	137	0.34	30	1.19	9	1.53	7
	32	0.06	161	0.13	76	0.60	17	0.80	13
32	1	0.35	29	2.49	5	1.89	6	3.96	3
	2	0.23	44	2.39	5	1.78	6	4.05	3
	4	0.15	65	1.71	6	1.80	6	4.22	3
	8	0.09	116	1.07	10	1.80	6	4.55	3
	16	0.07	150	0.41	25	1.64	7	2.55	4
	32	0.06	157	0.17	61	1.07	10	1.40	8